FIN LOADS AND CONTROL-SURFACE HINGE MOMENTS MEASURED IN FULL-SCALE WIND-TUNNEL TESTS ON THE X-24A FLIGHT VEHICLE

by Ming H. Tang and V. Michael DeAngelis

Flight Research Center
Edwards, Calif.

1. Report No. NASA TM X-1922	2. Government Accession No.	3. Recipient's Catalog No.		
4. Title and Subtitle FIN LOADS AND CONTROL-SURFACE HINGE MOMENTS MEASURED IN FULL-SCALE WIND-TUNNEL TESTS ON THE X-24A FLIGHT VEHICLE (U)		5. Report Date November 1969		
		6. Performing Organization Code		
7. Author(s) Ming H. Tang and V. Michael DeAngelis		8. Performing Organization Report No. H-580		
		10. Work Unit No. 727-00-00-01-24		
9. Performing Organization Name and Address NASA Flight Research Center P.O. Box 273 Edwards, California 93523		11. Contract or Grant No.		
		13. Type of Report and Period Covered Technical Memorandum		
12. Sponsoring Agency Name and Address National Aeronautics and Space Administration Washington, D.C. 20546		14. Sponsoring Agency Code		
15. Supplementary Notes				

16. Abstract (U)

Tests were conducted on the full-scale X-24A lifting body in the 40- by 80-Foot Wind Tunnel at the NASA Ames Research Center. One purpose of the tests was to measure aerodynamic loads on the stabilizing fins and hinge moments on all the control surfaces. The tests were conducted at dynamic pressures of 60, 80, and 100 lb/ft^2 (2870, 3830, and 4790 N/m^2). The effects of variations in rudder deflection, flap deflection, and angles of attack and sideslip were studied. Also, limited tests were performed with a simulated ablated coating over most of the vehicle to assess the effects of the ablated surface on the aerodynamic characteristics.

Detailed results of the wind-tunnel tests are given in the form of load coefficients and hinge-moment coefficients. The results are compared with data from tests performed in other wind tunnels on small-scale models.

17. Key Words Suggested by Author(s) X-24A lifting body Full-scale wind-tunnel loads		18. Distribution Statement Available to U.S. Government Agencies and Their Contractors Only		
19. Security Classif. (of this report) Confidential	20. Security Classif. (of this page) Unclassified		21. No. of Pages 34	22. Price

FIN LOADS AND CONTROL-SURFACE HINGE MOMENTS MEASURED IN

FULL-SCALE WIND-TUNNEL TESTS ON THE X-24A FLIGHT VEHICLE*

By Ming H. Tang and V. Michael DeAngelis
Flight Research Center

INTRODUCTION

The development of maneuverable vehicles capable of controlled reentry from earth orbit to a tangential landing led to the construction of three manned lifting-body configurations to investigate flight controllability in the terminal recovery area. (See refs. 1 and 2.) One of these vehicles is the X-24A, currently being flight tested at the NASA Flight Research Center.

The design of the X-24A was based more heavily on configurational test results than is usual for most flight vehicles. Because the configuration is different from that of conventional aircraft, there was little design precedent upon which to rely. The final design was the result of an evolutionary process which combined engineering judgment and theoretical studies with the results of numerous wind-tunnel tests on small-scale models. Consequently, as part of the preparation for a flight-test program, it was deemed advisable to conduct tests on the full-scale vehicle in the 40- by 80-Foot Wind Tunnel at the NASA Ames Research Center. A portion of the tests was performed to measure aerodynamic loads on the stabilizing fins and hinge moments on all the control surfaces. Loads measurements were made with strain-gage instrumentation. Generally, the tests were conducted at a Mach number of 0.25. In addition, tests were made with a simulated ablated coating on the fuselage and outer portions of the outboard fins to assess the effect of the ablated surface on aerodynamic characteristics, including fin loads and control-surface hinge moments.

This report presents the loads measurements from the full-scale wind-tunnel tests and compares the results with data from previous tests on 8-percent-scale models in other wind tunnels. The comparisons show the agreement between full-scale and small-scale tests and may help to establish a level of confidence in the structural design of the vehicle.

SYMBOLS

Measurements for this investigation were taken in the U.S. Customary System of Units. Equivalent values are indicated herein in the International System of Units (SI). Details concerning the use of SI, together with physical constants and conversions, are given in reference 3.

---

*Title, Unclassified.

B	fin bending moment, in-lb (m-N)
b	reference span, in. (m)
C_B	fin bending-moment coefficient, $\dfrac{B}{qSb}$
C_h	control-surface hinge-moment coefficient, $\dfrac{H}{qS\bar{c}}$
C_N	fin normal-force coefficient, $\dfrac{N}{qS}$
C_T	fin torsion coefficient, $\dfrac{T}{qSc}$
c	mean aerodynamic chord, in. (m)
$\bar{c}$	average chord, in. (m)
H	hinge moment, in-lb (m-N)
M	free-stream Mach number
N	fin normal force, lb (N)
q	free-stream dynamic pressure, lb/ft^2 (N/m^2)
S	surface area, ft^2 (m^2)
T	fin torsion, in-lb (m-N)
V	relative wind, ft/sec (m/sec)
X, Y. Z	vehicle reference axes
α	vehicle angle of attack, deg

2

β vehicle angle of sideslip, deg

δ control-surface deflection, deg

δ_{au} differential upper-flap deflection (right roll positive)

Subscripts:

c   center fin

l lower flap

r   rudder

rb   rudder bias

rl lower rudder

ru   upper rudder

t   outboard fin

u   upper flap

DESCRIPTION OF THE X-24A VEHICLE

The X-24A research vehicle, installed in the 40- by 80-Foot Wind Tunnel at the NASA Ames Research Center, is shown in figure 1. The X-24A has a boattailed body with a thick midsection and a blunt nose, three stabilizing vertical fins, and eight control surfaces — four rudders and four flaps. A three-view drawing of the vehicle is shown in figure 2.

Two pairs of rudders, located at the trailing edges of the two outboard fins, can be moved symmetrically in bias with their trailing edges deflected either outward or inward from the zero position by an equal amount. In addition, the upper rudders may be deflected in unison (i.e., both rudders moving in the same direction) from the bias position to provide directional control. The two upper flaps and the two lower flaps may be deflected symmetrically for pitch and trim control. Either the upper flaps or the lower flaps may be deflected differentially for roll control.

A more detailed description of the X-24A vehicle is given in reference 4. Pertinent physical dimensions of the fins and control surfaces are listed in table I.

INSTRUMENTATION

Instrumentation for the wind-tunnel tests consisted of the wind-tunnel instrumentation, which measured the tunnel dynamic pressure and vehicle attitude, and the vehicle instrumentation. Vehicle instrumentation was connected to a pulse code modulation (PCM) system which telemetered the data to a nearby ground station for storage on magnetic tape. The wind-tunnel instrumentation was connected to the tunnel data-acquisition system (ref. 5).

The sign conventions for parameters used in this report are shown in figure 3.

Strain-Gage Instrumentation and Calibration

The left-hand outboard fin and the center fin (fig. 3(a)) each have three spars to transmit aerodynamic loads. Five strain-gage shear bridges and six strain-gage bending bridges were installed at the root region of the three spars of the outboard fin. Four shear bridges and four bending bridges were installed at the root region of the two forward spars of the center fin.

The outboard-fin instrumentation was calibrated by the conventional point-by-point procedure of reference 6. Loads were applied at 17 load points on the surface of the outboard fin. The center fin was calibrated by a distributed load technique. Approximately 75 percent of the area of the center fin was loaded by four separately controlled jacks acting through eight load pads. By regulating the forces applied by each of the jacks, the center of pressure of the combined load from all the jacks was moved to 27 different positions over an area bounded by 20 percent to 60 percent of the mean aerodynamic chord and by 40 percent to 60 percent of the span. A large number of bridge combinations were investigated by means of influence coefficient analysis to derive loads equations (ref. 6). The most accurate equations for shear, bending moment, and torque were selected for use with the wind-tunnel data.

The control-surface hinge-moment instrumentation consisted of strain-gage bending bridges mounted on the actuator mechanisms of the various control surfaces. The control-surface instrumentation was calibrated at several control positions by loading each surface in place on the aircraft and recording the outputs on a PCM system. A straight line fitted through the data points established the relationship between load and strain-gage output at each control-surface position.

Control-Surface-Position Instrumentation

The position of each control surface was measured by a control-position transducer which was calibrated in place on the vehicle with a template prior to the wind-tunnel test. Deflections of the rudders and flaps were taken as the average of the left-hand and right-hand surfaces.

ESTIMATED ERRORS

Estimates were made of the errors in each of the parameters pertinent to the presentation of the loads data. The vehicle's attitude and the dynamic-pressure errors were obtained from reference 5. The error in the control-surface position was estimated from ground-test results.

A probable error of resolution was determined for the shear, bending moment, and torque equations for the left-hand and center fins and the control-surface hinge moments. This resolution error is based on the PCM system error.

In addition to the resolution error, an equation error was calculated for the shear, bending moment, and torque of the left-hand and center fins. The equation errors are based on a check-load calibration performed immediately following the wind-tunnel tests.

Because the control-surface hinge moments were obtained from linear influence coefficients which were free of hysteresis, there are no relevant equation errors.

The estimated errors of the pertinent aircraft and load parameters are summarized in the following table:

Parameter	Error
α	$\pm 0.2°$
β	$\pm 0.3°$
δ	$\pm 0.3°$
q	± 0.5 percent
B_c —	
Probable error of resolution	160 in-lb (18.1 m-N)
Equation error	5 percent
B_t —	
Probable error of resolution	350 in-lb (39.6 m-N)
Equation error	8 percent
N_c —	
Probable error of resolution	24 lb (106.8 N)
Equation error	5 percent
N_t —	
Probable error of resolution	120 lb (533.8 N)
Equation error	8 percent
T_c —	
Probable error of resolution	360 in-lb (40.7 m-N)
Equation error	15 percent
T_t —	
Probable error of resolution	2100 in-lb (237.3 m-N)
Equation error	9 percent
Hinge-moment probable errors —	
Upper rudders	51 in-lb (5.8 m-N)
Lower rudders	76 in-lb (8.6 m-N)
Upper flaps	125 in-lb (14.1 m-N)
Right-hand lower flap	260 in-lb (29.4 m-N)

TEST PROCEDURE

The vehicle was mounted on struts in the test section of the 40- by 80-Foot Wind Tunnel. All the wind-tunnel tests discussed herein were performed with the landing-gear doors closed (fig. 1). The wind tunnel is described in reference 7.

The operating procedure was as follows: The control surfaces were set for a particular configuration, and the vehicle was rotated through a range of angles of attack from $0°$ to $20°$. Then the control-surface settings were changed, and the angle-of-attack range was again traversed. Generally, the tests were conducted at a Mach number of 0.25 and a dynamic pressure of 100 lb/ft^2 (4790 N/m^2). For a limited number of tests, the angle of sideslip and the dynamic pressure were varied; dynamic pressure ranged from 60 to 100 lb/ft^2 (2870 to 4790 N/m^2). Reynolds number varied from 1.52×10^6 per foot (4.99×10^6 per meter) to 2.17×10^6 per foot (7.12×10^6 per meter).

In order to simulate the vehicle with a reentry ablated shield in a post-reentry condition, a mixture of sand and glue was affixed to the outboard sides of the outboard fins and to the sides and bottom of the fuselage. A detailed description of the ablated test is presented in reference 8. Shear, bending moment, and torsion loads on the left-hand fin and hinge moments on the eight control surfaces were acquired for the ablated configuration.

The X-24A, with eight control surfaces, presents many possible combinations of control-surface settings and vehicle attitudes. In order to establish a reasonable number of configurations for the wind-tunnel tests, only control-surface settings which were likely to affect the loads significantly were considered. From these, configurations were selected which were within the range of control-surface settings and vehicle attitudes most likely to be encountered during the manned flight-test program. Only one control-surface position or vehicle attitude was varied at a time in order to isolate the effect on the loads of a change in a particular condition.

RESULTS AND DISCUSSION

Results of the full-scale wind-tunnel tests are presented in figures 4 to 7, and the test conditions associated with these results are listed in the table on the following page.

Load Coefficients

Left-hand outboard fin. — The left-hand outboard-fin normal-force, bending-moment, and torsion coefficients are plotted against angle of attack in figure 4. In general, the figure shows that increasing the angle of attack increased the normal-force and bending-moment coefficients. The torsion coefficient was not very sensitive to variation in angle of attack. Positive rudder bias and positive rudder deflections increased the outboard-fin normal-force and bending-moment coefficients and increased the negative values of the torsion coefficients, as shown in figures 4(a) to 4(c). Figure 4(d) illustrates that increasing the deflection of the upper flaps reduced the normal-force and bending-moment coefficients and had negligible effect on the torsion coefficient.

6

Coefficients presented	Figure number	q, lbf/ft² (N/m²)	Test conditions					
			Skin surface	β, deg	δ_u, deg	δ_{au}, deg	δ_l, deg	δ_{rb}, deg	δ_r, deg
Left-hand outboard fin									
C_{N_t}, C_{B_t}, C_{T_t} vs. α	4(a)	100 (4790)	Clean	0	−20	0	10	9, 0, −9	10
	4(b)	100 (4790)	Clean	0	−20	0	10	9, 0, −9	0
	4(c)	100 (4790)	Clean	0	−20	0	10	9, 0, −9	−10
	4(d)	100 (4790)	Clean	0	−3, −20, −30	0	0, 10, 20	0	0
	4(e)	100 (4790)	Clean	−6, 0, 6	−3	0	0	0	0
	4(f)	100 (4790)	Clean and ablated	0	−3	0	0	−9	0
	4(g)	60 (2870) / 80 (3830) / 100 (4790)	Clean	0	−20	0	10	−9	0
Center fin									
C_{N_c}, C_{B_c}, C_{T_c} vs. α	5(a)	60 (2870)	Clean	−6, 0, 6	−20	−20, 0, 20	10	0	0
	5(b)	100 (4790)	Clean	−6, 0, 6	−3	0	0	0	0
Upper and lower rudders									
$C_{h_{ru}}$, $C_{h_{rl}}$ vs. α	6(a)	100 (4790)	Clean	0	−20	0	10	9, 0, −9	10
	6(b)	100 (4790)	Clean	0	−20	0	10	9, 0, −9	0
	6(c)	100 (4790)	Clean	0	−20	0	10	9, 0, −9	−10
	6(d)	100 (4790)	Clean	0	−3, −20, −30	0	0, 10, 20	0	0
	6(e)	100 (4790)	Clean	−6, 0, 6	−3	0	0	0	0
	6(f)	100 (4790)	Clean and ablated	0	−3	0	0	−9	0
	6(g)	60 (2870) / 80 (3830) / 100 (4790)	Clean	0	−20	0	10	−9	0
Upper and lower flaps									
C_{h_u}, C_{h_l} vs. α	7(a)	100 (4790)	Clean	0	−20	0	10	9, 0, −9	0
	7(b)	100 (4790)	Clean	0	−3, −20, −30	0	0, 10, 20	0	0
	7(c)	100 (4790)	Clean	−6, 0, 6	−3	0	0	0	0
	7(d)	100 (4790)	Clean and ablated	0	−3	0	0	−9	0
	7(e)	60 (2870) / 80 (3830) / 100 (4790)	Clean	0	−20	0	10	−9	0

7

Although the effect was relatively small compared with that of the upper-flap deflections, the normal-force and bending-moment coefficients increased with increasing lower-flap deflections. The torsion coefficients were virtually insensitive to any changes in the lower-flap position (fig. 4(e)).. Figure 4(f) shows that the normal-force and bending-moment coefficients and the torsion coefficients increased in magnitude with increasing negative angles of sideslip. The effect of the simulated ablated coating and of varying dynamic pressure is shown in figure 4(g). The ablated coating caused a small increase in the normal-force coefficients but virtually no change in the bending-moment and torsion coefficients. The normal-force coefficient and the torsion coefficient increased slightly and the bending-moment coefficient decreased slightly with increasing dynamic pressure.

Center fin. — The center-fin normal-force, bending-moment, and torsion coefficients are plotted versus angle of attack in figure 5. In general, the center-fin loads were insensitive to changes in angle of attack. Figure 5(a) shows that negative δ_{au} resulted in an increase in the normal-force and bending-moment coefficients and an increase in the negative values of the torsion coefficients. Figure 5(b) shows that both normal-force and bending-moment coefficients increased with increasing negative sideslip angle. The torsion coefficient did not vary with changes in sideslip angle. The effect of variation in dynamic pressure was investigated for a symmetrical configuration only. Because the center-fin loads depended on an asymmetric configuration, no data were available on the effect of dynamic pressure on the center fin.

Hinge-Moment Coefficients

Rudders. — The upper- and lower-rudder hinge-moment coefficients are plotted versus angle of attack in figure 6. Increasing the angle of attack increased the rudder hinge-moment coefficients in most cases. Figures 6(a) to 6(c) show that positive rudder bias increased both the upper- and the lower-rudder hinge-moment coefficients in the positive direction. Positive rudder deflection increased the left-hand upper-rudder hinge-moment coefficients and decreased the right-hand upper-rudder hinge-moment coefficients. Rudder deflections had negligible effect on the lower-rudder hinge-moment coefficients. The upper-rudder hinge-moment coefficients increased with decreasing magnitude of upper-flap deflections (fig. 6(d)). The lower-rudder hinge-moment coefficients were insensitive to upper-flap deflections. Only the upper-rudder hinge-moment coefficients showed an increase due to an increase in lower-flap deflection (fig. 6(e)). Figure 6(f) shows that increasing the sideslip angle increased the right-hand and decreased the left-hand upper-rudder hinge-moment coefficients. Lower-rudder hinge-moment coefficients were relatively insensitive to variations in sideslip angle. In general, both the ablated coating and the increase in dynamic pressure slightly increased the upper-rudder hinge-moment coefficients and had virtually no effect on the lower-rudder hinge-moment coefficients (fig. 6(g)).

Flaps. — The left- and right-hand upper-flap and the right-hand lower-flap hinge-moment coefficients are plotted versus angle of attack in figure 7; the left-hand lower-flap instrumentation was inoperative during the tests. Figure 7(a) shows that the upper-flap hinge-moment coefficients were not sensitive to changes in angle of attack nor to variation in rudder bias. The lower-flap hinge-moment coefficients increased with increasing angle of attack but were not sensitive to rudder bias. Both the upper- and the lower-flap hinge-moment coefficients were insensitive to rudder deflections; hence,

no data are presented. The upper-flap hinge-moment coefficients increased with increasing magnitude of upper-flap deflection (fig. 7(b)). The lower-flap hinge-moment coefficients were essentially insensitive to upper-flap deflections. Figure 7(c) shows that the upper-flap hinge-moment coefficients were insensitive to changes in lower-flap deflection. The lower-flap hinge-moment coefficients increased with increasing lower-flap deflections and increasing angle of attack. Both the upper- and the lower-flap hinge-moment coefficients were virtually insensitive to any changes in sideslip angle (fig. 7(d)). Figure 7(e) shows that both the ablated coating and the dynamic-pressure variation had essentially no effect on the flap hinge-moment coefficients.

COMPARISON OF THE FULL-SCALE WITH THE 8-PERCENT-SCALE X-24A FIN LOADS AND CONTROL-SURFACE HINGE MOMENTS

Data obtained from the full-scale tests reported herein were compared, where possible, with similar results from previous tests on small-scale models in other wind tunnels. Many of the earlier models tested were configurations significantly different from the final full-scale vehicle, and tests on such models were not considered for comparative purposes. However, two series of tests — one at the Cornell Aeronautical Laboratory (ref. 4), the other in the 8-foot transonic pressure tunnel at the NASA Langley Research Center (ref. 9) — were made on models with configurations very similar to that of the actual vehicle. One model had slightly different canopy dimensions, but the difference is believed to be too small to have any important effect on the aerodynamic loads. The comparisons presented herein are made with data from references 4 and 9.

As might be expected, the results from the different series of tests were not on a directly comparable basis, and some manipulation was required to make them comparable. Aside from the size of the test specimens, the major differences were Mach number, instrumentation, type of model support, and control-surface settings. The full-scale tests generally were made at a Mach number of 0.25 with strain-gage instrumentation and with the vehicle mounted on pylon supports. The 8-percent-scale tests discussed herein were made at a Mach number of 0.60 with pressure sensors and the models supported by stings. Some of the differences were eliminated by making the comparisons on the basis of dimensionless coefficients. No corrections were made for differences in model support. To bring the control-surface settings into agreement, straight-line interpolation of the full-scale data was used. Because the small-scale tests did not include bending-moment or torsion data, comparisons are confined to normal-force and hinge-moment coefficients. The results are shown graphically in figures 8 to 11, and the test conditions associated with the data in these figures are presented in the table on the following page.

Load Coefficients

Left-hand outboard fin. – In figure 8 the left-hand outboard-fin normal-force coefficient is plotted against angle of attack. In general, the change in normal-force coefficient with change in angle of attack shown by the full-scale and the 8-percent-scale data agreed except at higher angles of attack. Figure 8(a) shows that the normal-force coefficients obtained from the two tests agreed at angles of attack from $0°$ to $12°$.

Table: Test conditions

Coefficients presented	Figure number	Full scale						8-percent-scale					
		M	β, deg	δ_u, deg	δ_l, deg	δ_rb, deg	δ_r, deg	M	β, deg	δ_u, deg	δ_l, deg	δ_rb, deg	δ_r, deg
Left-hand outboard fin													
C_{N_t} vs. α	8(a)	0.25	-6, 0, 6	-20, -30	20	0	0	0.6	-5, 0, 5	-20, -30	20	0	0
	8(b)	.25	0	-30	10, 20	0	0	.6	0	-30	10, 20	0	0
	8(c)	.25	0	-30	20	5, 0, -5	0	.6	0	-30	20	5, 0, -5	0
Center fin													
C_{N_c} vs. α	9	0.25	-6, 6	-3	0	0	0	0.6	-5, 5	-30	20	0	0
Upper and lower rudders													
$C_{h_{ru}}$, $C_{h_{rl}}$ vs. α	10(a)	0.25	0	-20, -30	10, 20	0	0	0.6	0	-20, -30	10, 20	0	0
	10(b)	.25	0	-30	20	-5, 0, 5	0	.6	0	-30	20	5, 0, -5	0
	10(c)	.25	-6, 0, 6	-30	20	0	0	.6	-5, 0, 5	-30	20	0	0
Upper and lower flaps													
C_{h_u}, C_{h_l} vs. α	11(a)	0.25	0	-30, -20	20, 10	0	0	0.6	0	-30, -20	20, 10	0	0
	11(b)	.25	0	-30	20	-5, 5	0	.6	0	-30	20	-5, 5	0
	11(c)	.25	-6, 6	-30	20	0	0	.6	-5, 5	-30	20	0	0

10

Above 12° the difference may be due to the onset and propagation of flow separation, perhaps influenced by the difference in Mach number and Reynolds number between the full-scale and the 8-percent-scale tests. (The Reynolds numbers for the 8-percent-scale-model tests ranged from 4.4×10^6 to 8.9×10^6).

Figure 8(b) compares the effect of upper- and lower-flap deflections on the outboard-fin normal-force coefficient shown in the full-scale and the 8-percent-scale tests. In general, the coefficients from the two tests agreed. Figure 8(c) illustrates the effect of varying rudder bias from 5° to -5° on the outboard-fin normal-force coefficient. The coefficients from the full-scale and the 8-percent-scale tests agreed reasonably well; only at an angle of attack of 16° did they differ significantly.

Center fin. — Figure 9 shows the center-fin normal-force coefficients plotted against angle of attack. A comparison of the effect of sideslip-angle variation on the center-fin load showed that the change in normal-force coefficient due to a change in sideslip angle was relatively small in both the full-scale and the small-scale tests. In general, the full-scale normal-force coefficients were slightly larger in magnitude than those from the 8-percent-scale-model tests. The small differences may be due in part to differences in flap setting, sideslip angles, and Mach number between the full-scale tests and the model tests.

Hinge-Moment Coefficients

Rudders. — The left-hand upper- and lower-rudder hinge-moment coefficients are plotted against angle of attack in figure 10. Figure 10(a) shows the effect of upper- and lower-flap deflections on the rudder hinge-moment coefficients. The full-scale and 8-percent-scale hinge-moment coefficients compared reasonably well at angles of attack from 0° to 12° but showed poorer agreement from 12° to 20°. The effect of varying rudder bias on the rudder hinge-moment coefficients is shown in figure 10(b). Both the upper- and the lower-rudder hinge-moment coefficients from the full-scale vehicle were slightly more positive than the coefficients from the 8-percent-scale models and showed similar effects due to variation of rudder bias. Figure 10(c) shows the effect of sideslip-angle variation on the upper- and lower-rudder hinge-moment coefficients. The effect of sideslip-angle variation in the full-scale tests was greater for the upper-rudder and smaller for the lower-rudder hinge-moment coefficients than in the 8-percent-scale tests.

Flaps. — The upper- and lower-flap hinge-moment coefficients are plotted versus angle of attack in figure 11. Only the right-hand lower-flap hinge-moment data were available from the full-scale tests. Because the data presented are from symmetrical configurations, the full-scale right-hand lower-flap hinge-moment data were compared with the left-hand lower-flap hinge-moment data from the small-scale tests. The variation of flap hinge-moment coefficient with change in angle of attack was similar in the full-scale and the small-scale data. However, the magnitudes of the full-scale coefficients were somewhat lower than the magnitudes indicated by the small-scale tests. Figure 11(a) indicates that the change in flap hinge-moment coefficients due to flap deflection was smaller for the full-scale than for the 8-percent-scale tests. Figure 11(b) shows that rudder bias had no effect on either the upper- or the lower-flap hinge-moment coefficients. Only the upper-flap hinge-moment coefficients were affected by varying the sideslip angle (fig. 11(c)).

CONCLUSIONS

Aerodynamic loads data were obtained from full-scale wind-tunnel tests of the X-24A research vehicle. Results from the tests showed that:

1. The left-hand outboard-fin normal-force coefficient and bending-moment coefficient increased with increase in angle of attack, increase in negative angle of sideslip, decrease in upper-flap deflection, increase in lower-flap deflection, positive rudder bias, and positive rudder deflection.

2. The center-fin normal-force coefficient and bending-moment coefficient increased with increase in negative angle of sideslip and increase in negative differential upper-flap deflection.

3. The upper- and lower-rudder hinge-moment coefficients were sensitive to the same parameters as the outboard fin.

4. The upper-flap hinge-moment coefficients were relatively insensitive to changes in angle of attack, angle of sideslip, lower-flap deflection, or rudder bias and sensitive only to a variation of upper-flap deflection.

5. The lower-flap hinge-moment coefficients were sensitive primarily to changes in angle of attack and lower-flap deflections.

6. A simulated ablated coating applied to most of the vehicle surface to assess effects on aerodynamic characteristics tended to increase slightly the normal-force coefficient on the outboard fin and had negligible effect on the control-surface hinge-moment coefficients.

7. In general, the stabilizing-fin load coefficients and the control-surface hinge-moment coefficients agreed reasonably well with comparable loads data obtained from wind-tunnel tests of 8-percent-scale models.

REFERENCES

1. Thompson, Milton O.; Peterson, Bruce A.; and Gentry, Jerauld R.: Lifting-Body Flight Test Program. SETP Technical Review, second 1966 issue, vol. 8, no. 2, Sept. 1966, pp. 1-22.

2. Normyle, William J.: Manned Flight Tests to Seek Lifting-Body Technology. Aviation Week & Space Technology, vol. 84, no. 20, May 16, 1966, pp. 64-65, 67, 69, 71, 75.

3. Mechtly, E. A.: The International System of Units - Physical Constants and Conversion Factors. NASA SP-7012, 1964.

4. Stouffer, C. G.; and Hutton, B. L.: Transonic Pressure Test Results of an 8% Scale SV-5P Vehicle Tested at Cornell Aeronautical Laboratory, Inc., 8-Foot Wind Tunnel. Eng. Rep. No. 14113, vol. II, Martin Co., March 1966.

5. Mort, Kenneth; and Gamse, Berl: Full-Scale Wind-Tunnel Investigation of the Aerodynamic Characteristics of the M2-F2 Lifting-Body Flight Vehicle. NASA TM X-1588, 1968.

6. Skopinski, T. H.; Aiken, William S., Jr.; and Houston, Wilber B.: Calibration of Strain-Gage Installations in Aircraft Structures for the Measurement of Flight Loads. NACA Rep. 1178, 1954.

7. Anon.: Characteristics of Six Research Wind Tunnels of the Ames Aeronautical Laboratory. NACA, 1957.

8. Pyle, Jon S.; and Montoya, Lawrence C.: Effect of Roughness of Simulated Ablated Material on Low-Speed Performance Characteristics of a Lifting-Body Vehicle. NASA TM X-1810, 1969.

9. Brand, S.; and Blake, W. W.: Transonic Test Results From a Force, Moment, Pressure and Control Surface Hinge Moment Investigation Conducted With an 8% Scale SV-5P Vehicle in the NASA-Langley 8-Foot Transonic Pressure Wind Tunnel. Eng. Rep. No. 13683 (ASTIA No. AD-360 599), vol. IV, Martin Co., May 1965.

TABLE I. – REFERENCE AREAS AND DIMENSIONS OF THE FULL-SCALE X-24A FINS
AND CONTROL SURFACES

Center vertical fin, (airfoil slab) –
Area, ft^2 (m^2) 14.7 (1.37)
Mean aerodynamic chord, in. (m) 57.9 (1.47)
Root chord, in. (m) 73.9 (1.88)
Tip chord, in. (m) 38.0 (0.96)
Distance between root chord and mean aerodynamic
chord, in. (m) 17.3 (0.44)
Span, in. (m) 38.8 (0.99)
Outboard vertical fin (airfoil cambered with leading-edge droop) –
Area, each, ft^2 (m^2) 24.9 (2.31)
Mean aerodynamic chord, in. (m) 77.4 (1.97)
Root chord, in. (m) 101.9 (2.59)
Tip chord, in. (m) 45.7 (1.16)
Distance between root chord and mean aerodynamic
chord, in. (m) 21.3 (0.54)
Span, in. (m) 46.6 (1.18)
Upper rudder –
Area, each, ft^2 (m^2) 4.99 (0.46)
Chord, in. (m) 29.6 (0.75)
Span, in. (m) 24.2 (0.62)
Lower rudder –
Area, each, ft^2 (m^2) 6.67 (0.62)
Chord, in. (m) 29.6 (0.75)
Span, in. (m) 32.4 (0.82)
Upper flap –
Area, each, ft^2 (m^2) 10.82 (1.01)
Chord, in. (m) 34.1 (0.87)
Span, in. (m) 45.7 (1.16)
Lower flap –
Area, each, ft^2 (m^2) 13.99 (1.30)
Chord, in. (m) 44.9 (1.14)
Span, in. (m) 44.9 (1.14)
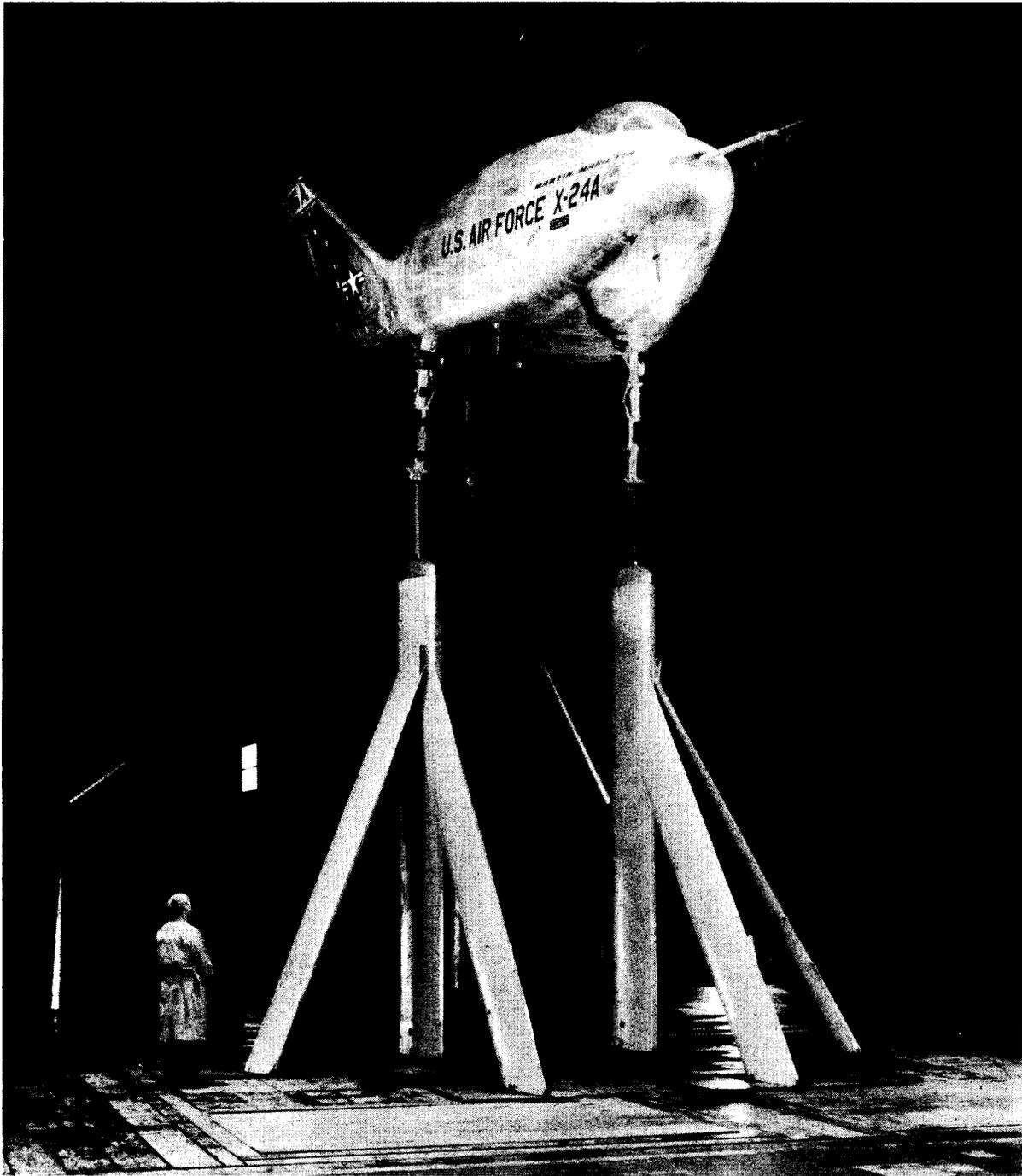
(a) Three-quarter front view.

A-40423-6

Figure 1.— X-24A flight vehicle mounted in the Ames 40- by 80-Foot Wind Tunnel.
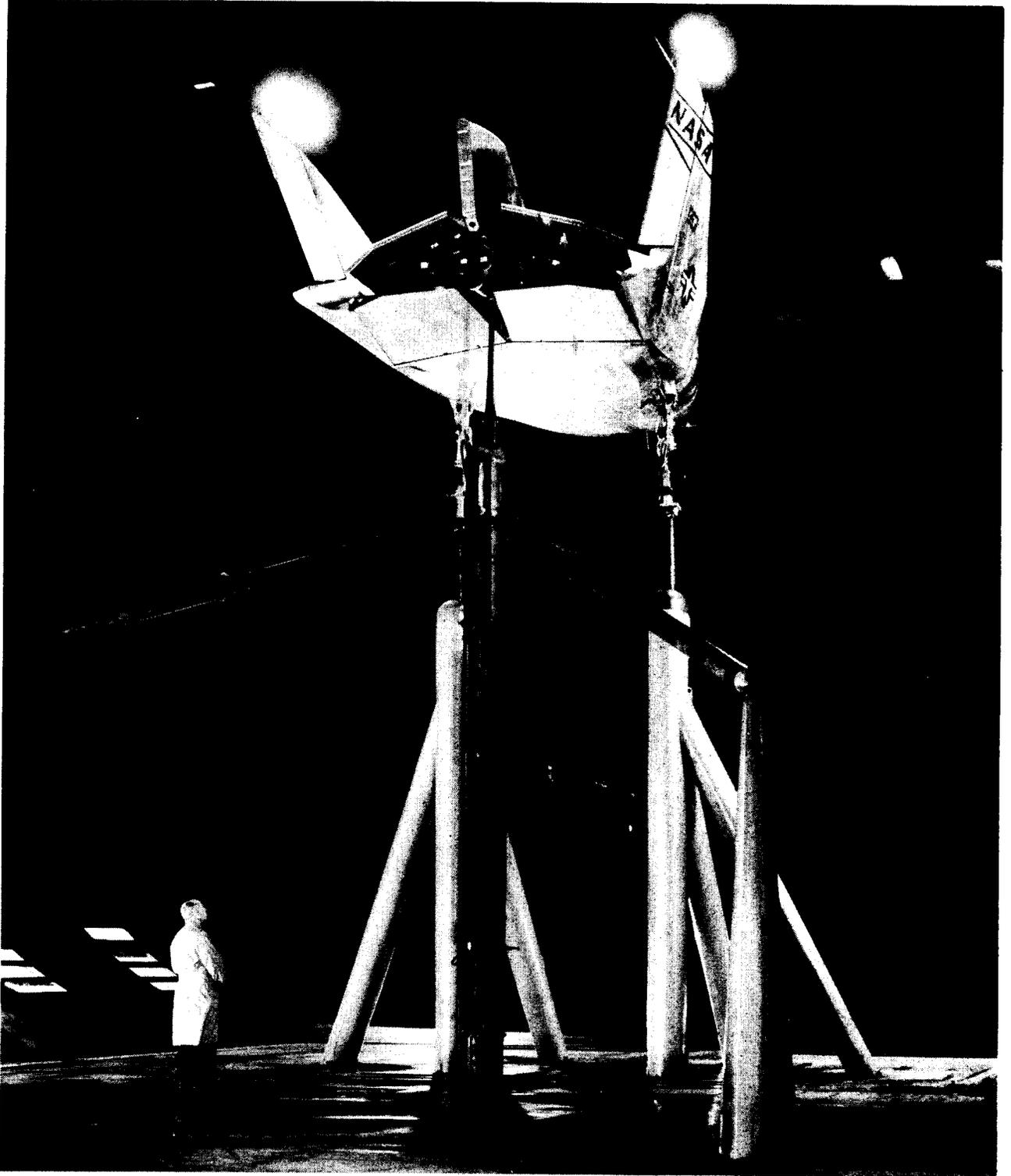
(b) Three-quarter rear view.
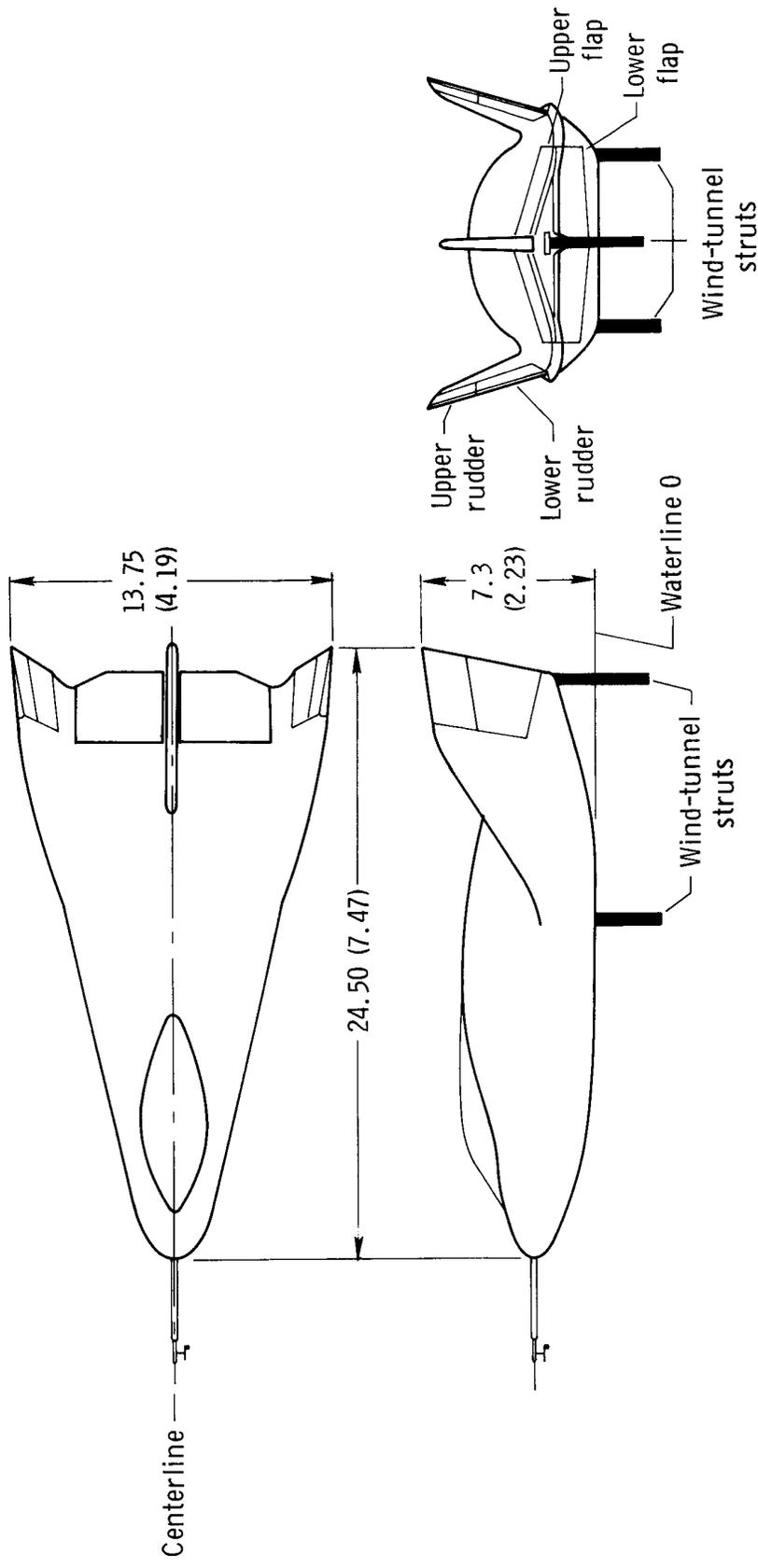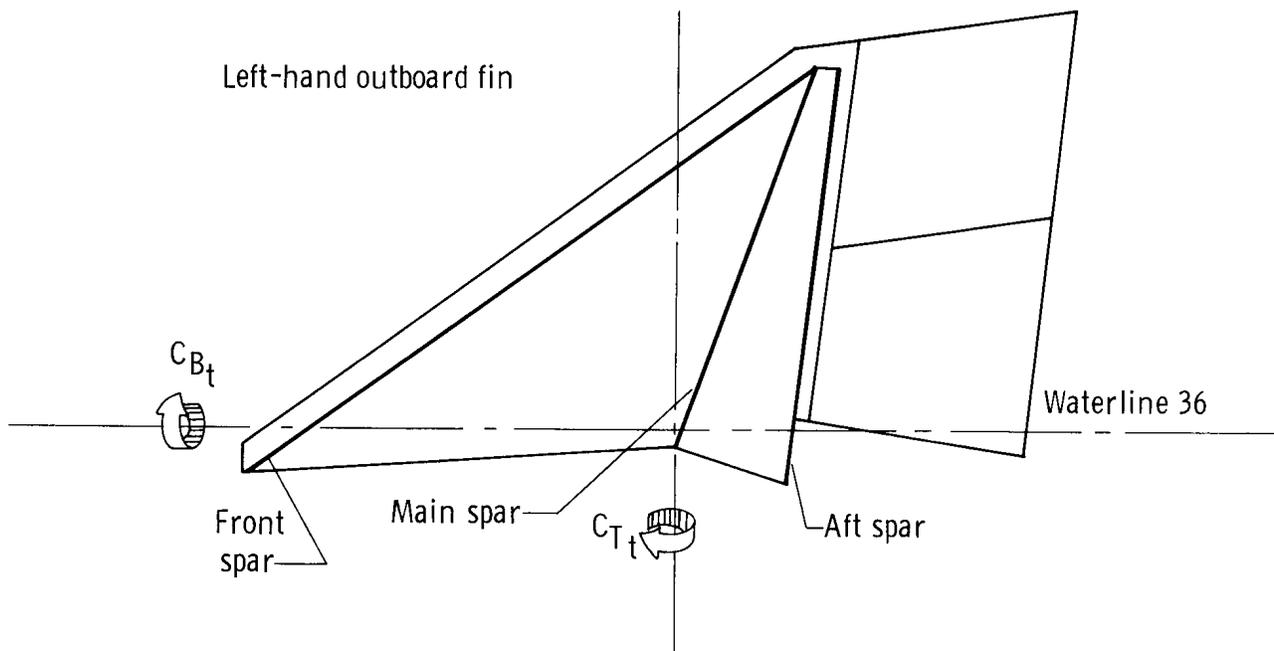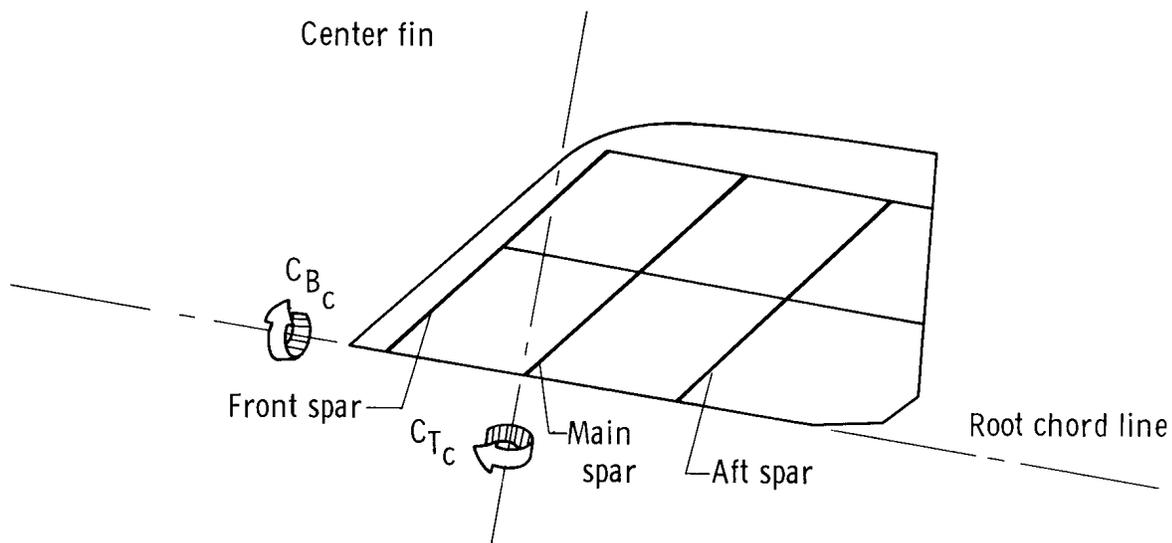
Figure 1.– Concluded.

A-40423-8

Figure 2.— *Three-view drawing of the X-24A lifting body on the wind-tunnel struts. Dimensions in feet (meters).*

Upper flap
Lower flap
Wind-tunnel struts
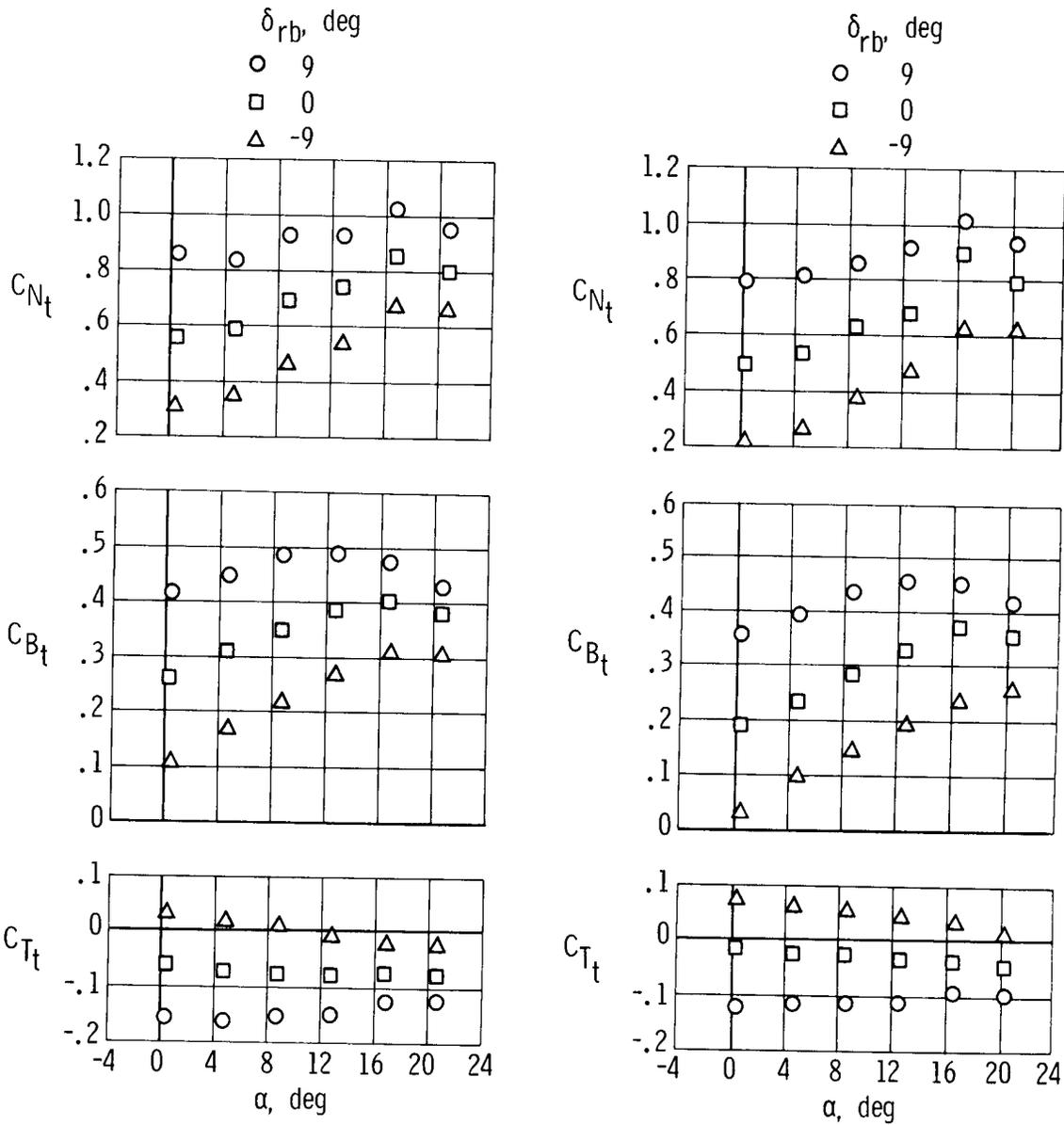Upper rudder
Lower rudder
Waterline 0

13.75 (4.19)
7.3 (2.23)
24.50 (7.47)
Wind-tunnel struts
Centerline

17

Left-hand outboard fin

C_{B_t}

Waterline 36

Front spar

Main spar

C_{T_t}

Aft spar

C_{N_c} and C_{N_t} positive in Y-direction (see fig. 3(b))

Center fin

C_{B_c}

Front spar

C_{T_c}

Main spar

Aft spar

Root chord line

(a) Left-hand outboard-fin and center-fin loads.

Figure 3.— Sign convention for the X-24A vehicle.

(b) Control-surface deflections and hinge moments.

Figure 3.— Concluded.

(a) Rudder-bias effect; $q = 100$ lb/ft^2 (4790 N/m^2); $\beta = 0^o$; $\delta_u = -20^o$; $\delta_{au} = 0^o$; $\delta_l = 10^o$; $\delta_r = 10^o$.

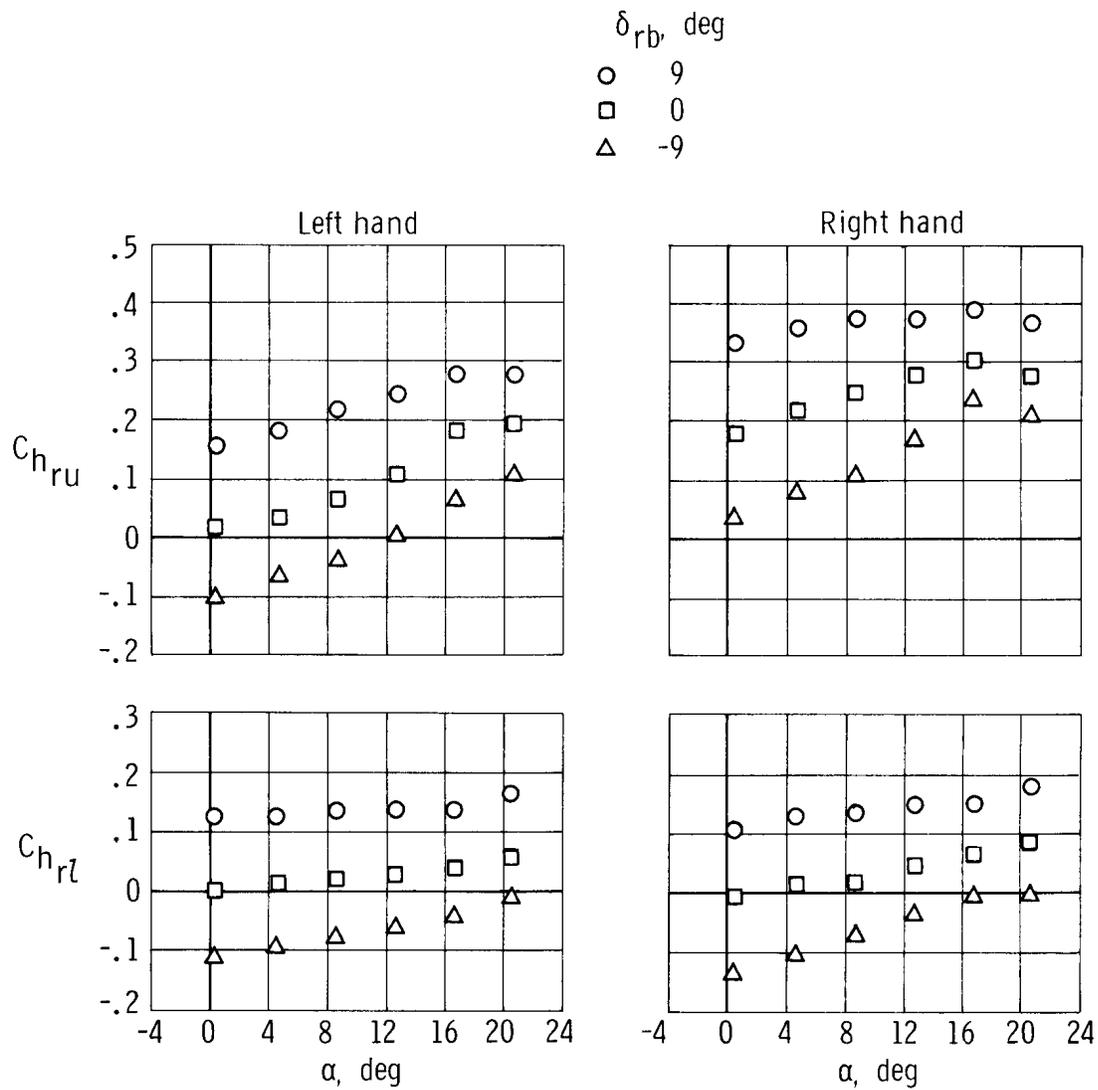b) Rudder-bias effect; $q = 100$ lb/ft^2 (4790 N/m^2); $\beta = 0^o$; $\delta_u = -20^o$; $\delta_{au} = 0^o$; $\delta_l = 10^o$; $\delta_r = 0^o$.

Figure 4.— Variation of left-hand outboard-fin normal-force, bending-moment, and torsion coefficients with angle of attack.
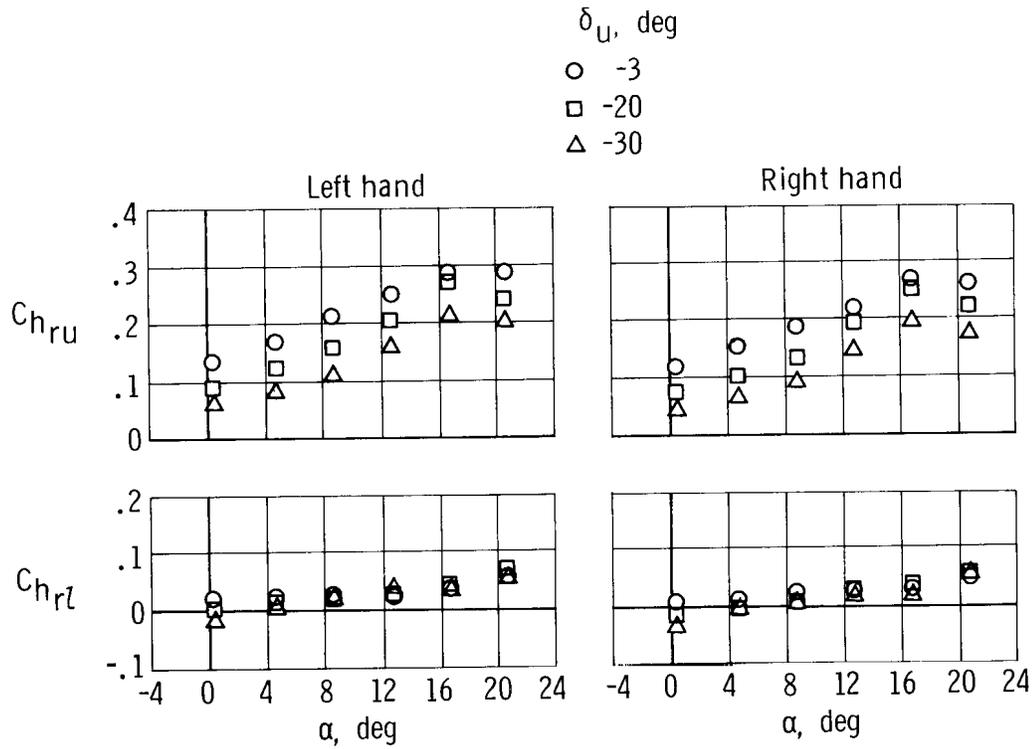
(c) Rudder-bias effect; $q = 100 \ lb/ft^2 \ (4790 \ N/m^2)$;
$\beta = 0^o$; $\delta_u = -20^o$; $\delta_{au} = 0^o$; $\delta_l = 10^o$; $\delta_r = -10^o$.

(d) Upper-flap effect; $q = 100 \ lb/ft^2 \ (4790 \ N/m^2)$;
$\beta = 0^o$; $\delta_{au} = 0^o$; $\delta_l = 0^o$; $\delta_{rb} = 0^o$; $\delta_r = 0^o$.

Figure 4.-- Continued.
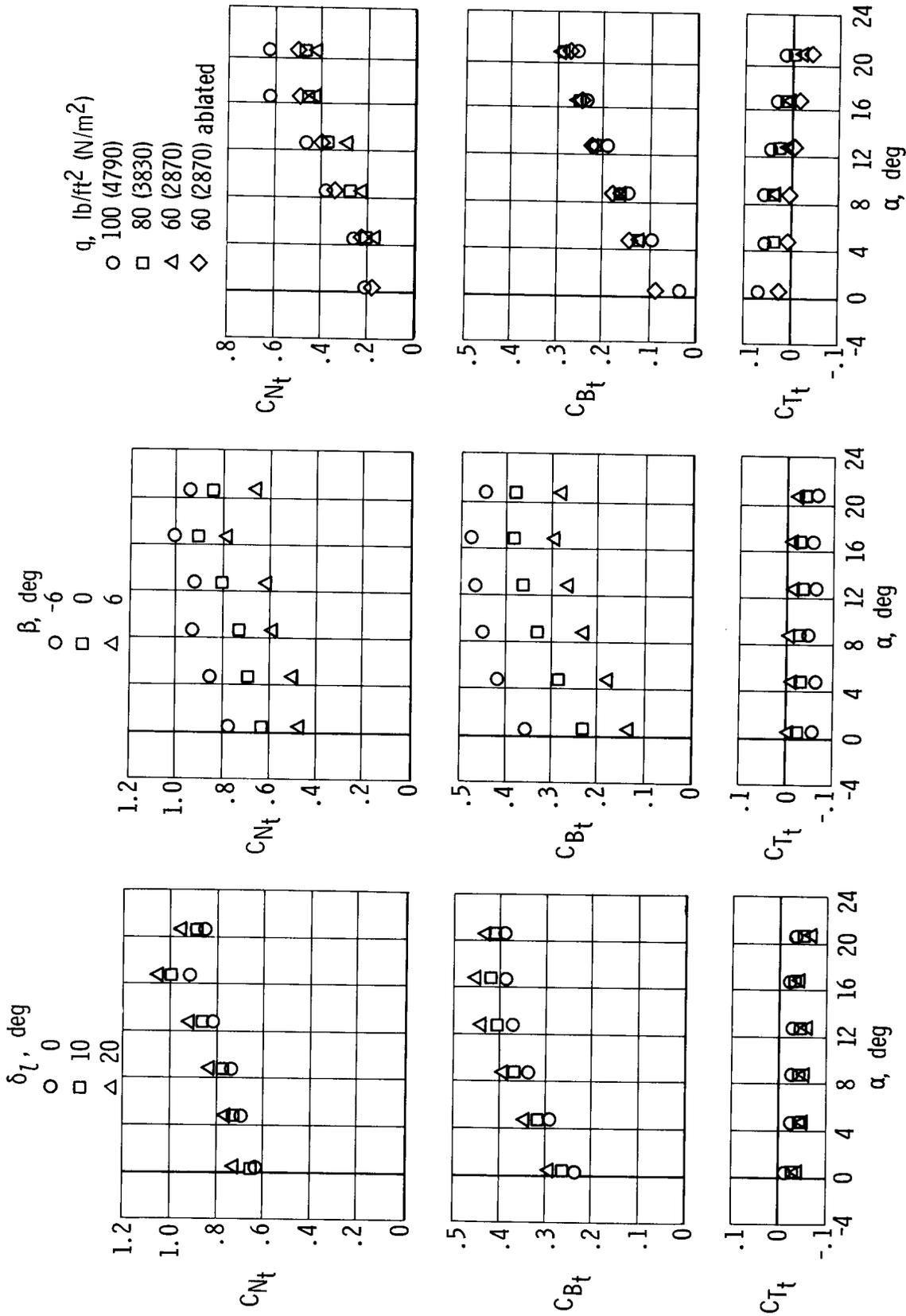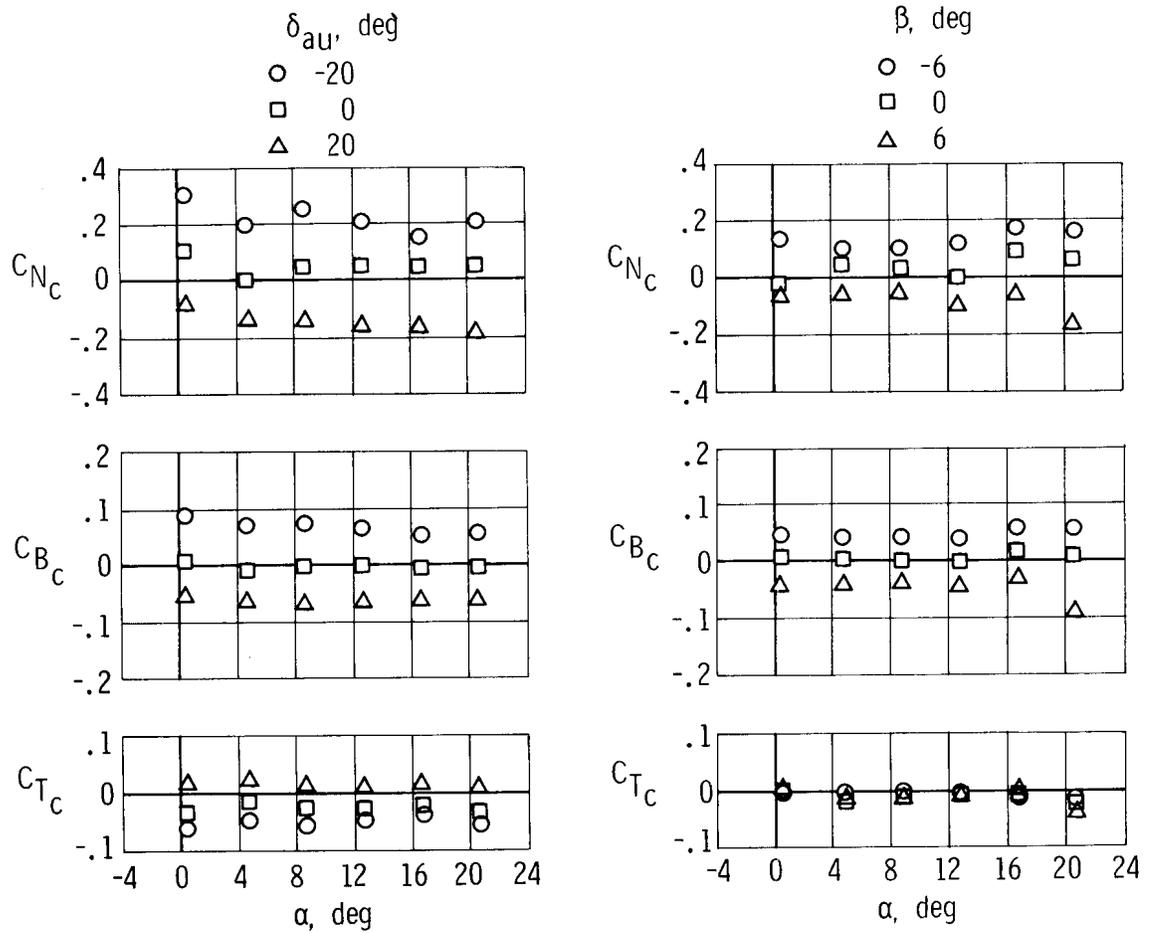
(e) Lower-flap effect; $q = 100$ lb/ft^2 (4790 N/m^2); $\beta = 0^o$; $\delta_u = -3^o$; $\delta_{au} = 0^o$; $\delta_{rb} = 0^o$; $\delta_r = 0^o$.

(f) Sideslip-angle effect; $q = 100$ lb/ft^2 (4790 N/m^2); $\delta_u = -3^o$; $\delta_{au} = 0^o$; $\delta_l = 0^o$; $\delta_{rb} = 0^o$; $\delta_r = 0^o$.

(g) Simulated ablated-coating and dynamic-pressure effect; $\beta = 0^o$; $\delta_u = -20^o$; $\delta_{au} = 0^o$; $\delta_l = 10^o$; $\delta_{rb} = -9^o$; $\delta_r = 0^o$.

Figure 4.– Concluded.

22

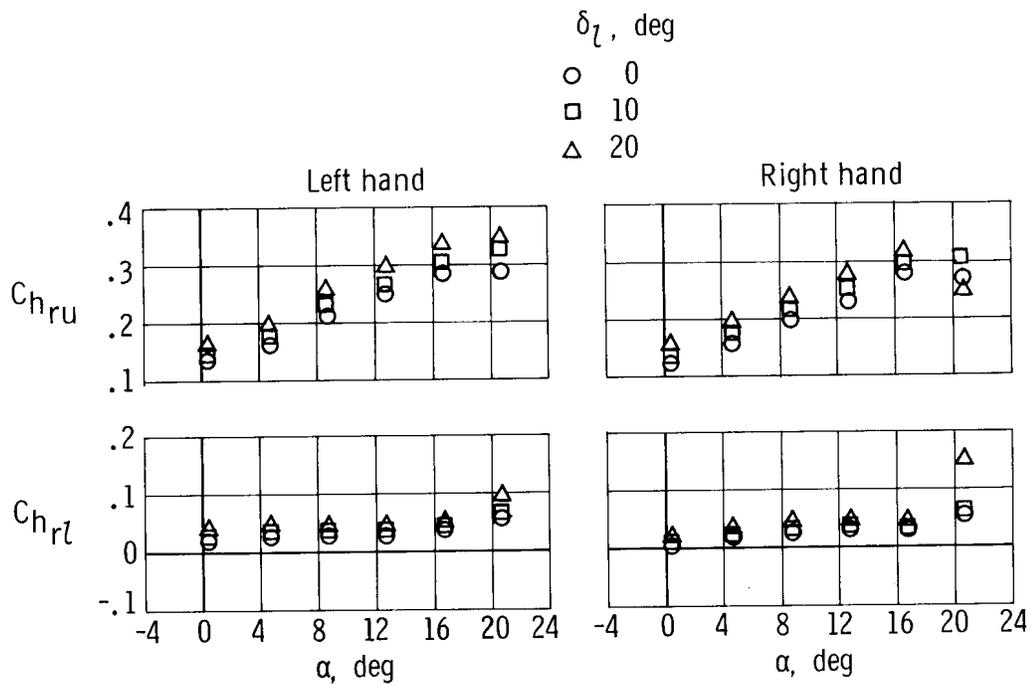*Figure 5.— Variation of center-fin normal-force, bending-moment, and torsion coefficients with angle of attack.*

23
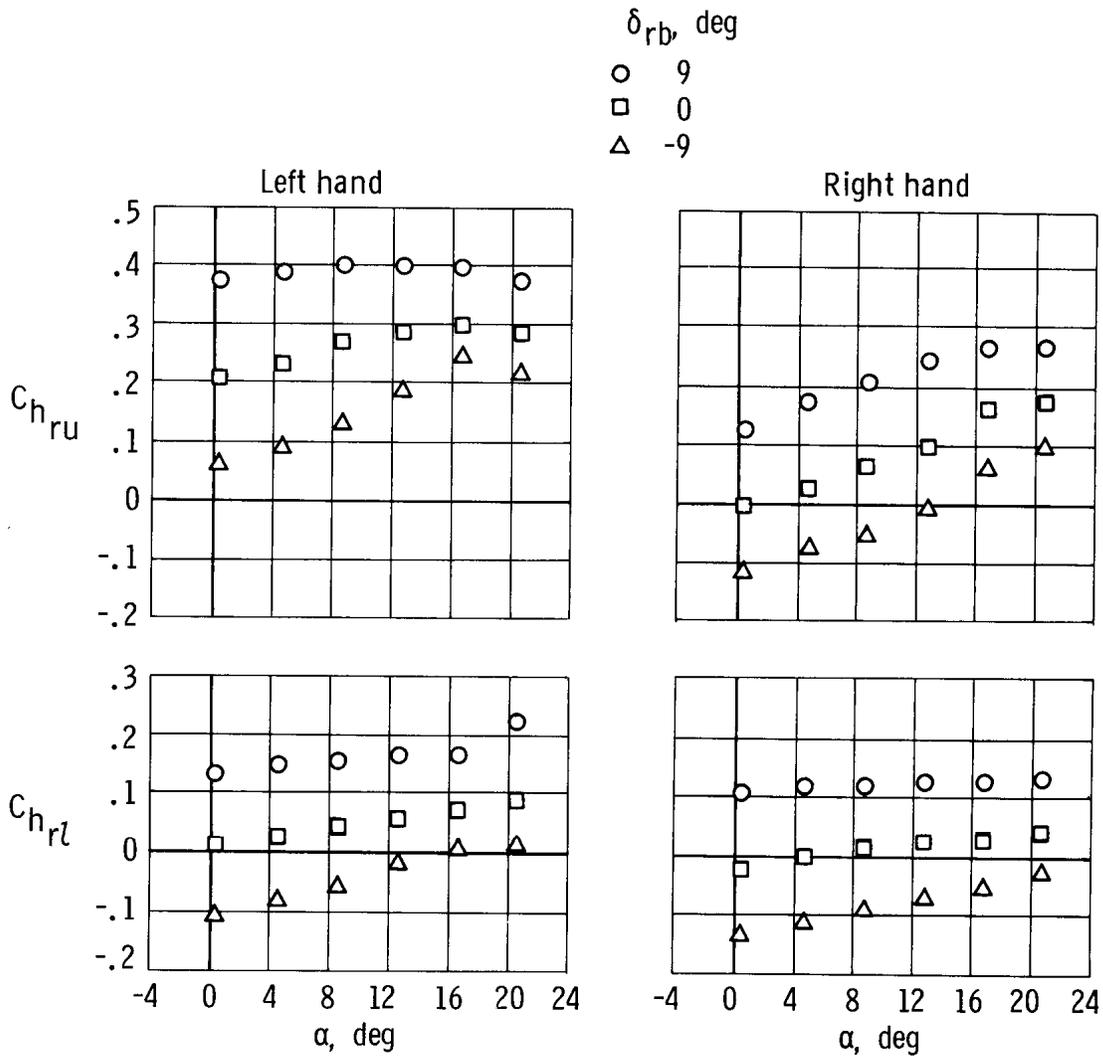
(a) Rudder-bias effect; $q = 100\ lb/ft^2$ $(4790\ N/m^2)$; $\beta = 0^o$; $\delta_u = -20^o$; $\delta_{au} = 0^o$; $\delta_l = 10^o$; $\delta_r = 10^o$.

Figure 6.— Variation of upper- and lower-rudder hinge-moment coefficients with angle of attack.

24
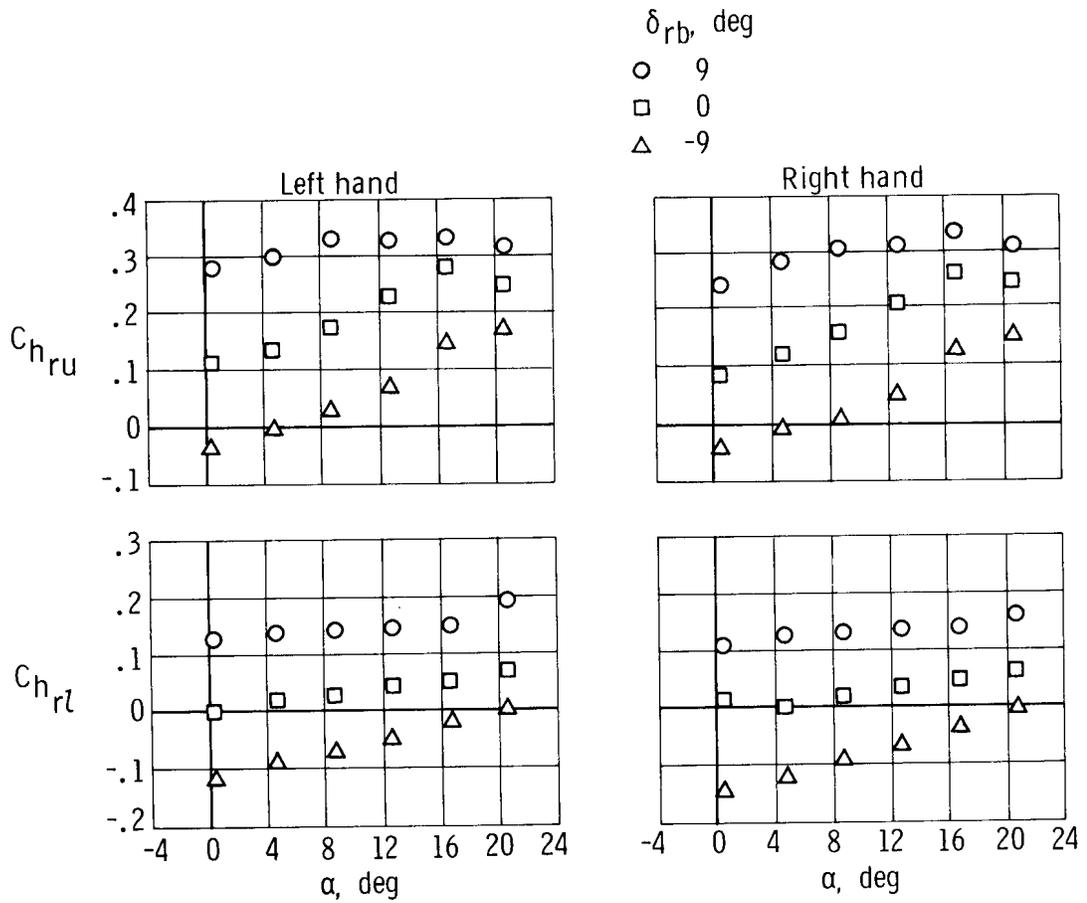
(b) Rudder-bias effect; $q = 100 \ lb/ft^2 \ (4790 \ N/m^2)$; $\beta = 0^o$; $\delta_u = -20^o$; $\delta_{au} = 0^o$; $\delta_\lambda = 10^o$; $\delta_r = 0^o$.

Figure 6.— Continued.

(c) Rudder-bias effect; $q = 100 \; lb/ft^2 \; (4790 \; N/m^2)$; $\beta = 0^o$; $\delta_u = -20^o$; $\delta_{au} = 0^o$; $\delta_l = 10^o$; $\delta_r = -10^o$.

Figure 6.-- Continued.

δ_u, deg
○ -3
□ -20
△ -30

Left hand   Right hand

.4
.3
$C_{h_{ru}}$ .2
.1
0

.2
.1
$C_{h_{rl}}$ 0
-.1
-4 0 4 8 12 16 20 24
α, deg

(d) Upper-flap effect; $q = 100\ lb/ft^2\ (4790\ N/m^2); \beta = 0^o;\ \delta_{au} = 0^o;\ \delta_l = 0^o;\ \delta_{rb} = 0^o;\ \delta_r = 0^o.$

δ_l, deg
○ 0
□ 10
△ 20

Left hand   Right hand

.4
.3
$C_{h_{ru}}$ .2
.1

.2
.1
$C_{h_{rl}}$ 0
-.1
-4 0 4 8 12 16 20 24
α, deg

(e) Lower-flap effect; $q = 100\ lb/ft^2\ (4790\ N/m^2); \beta = 0^o;\ \delta_u = -3^o;\ \delta_{au} = 0^o;\ \delta_{rb} = 0^o;\ \delta_r = 0^o.$

Figure 6.— Continued.

27
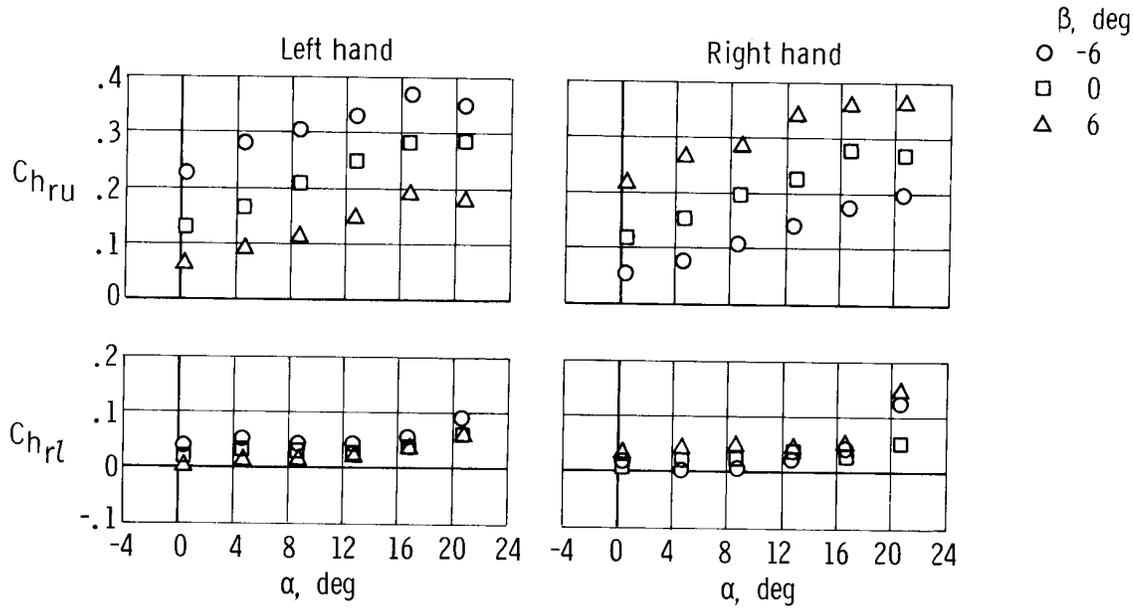
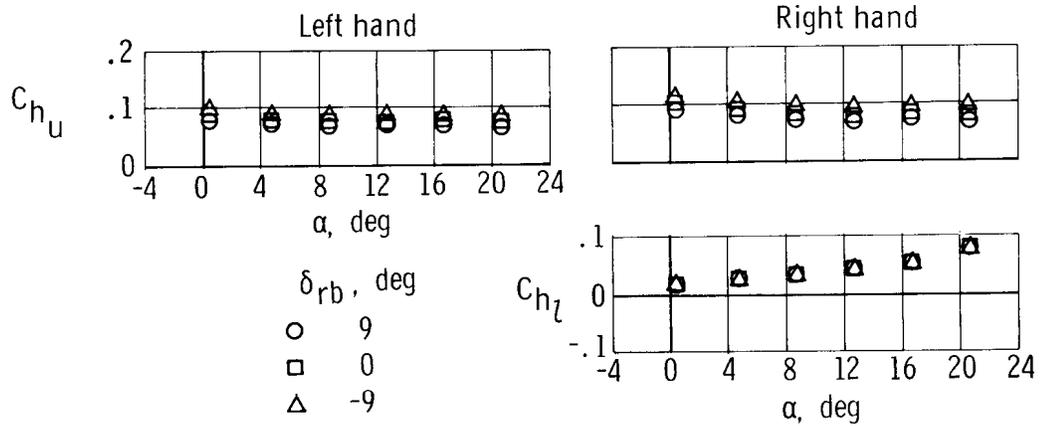(f) Sideslip-angle effect; $q = 100 \ lb/ft^2 \ (4790 \ N/m^2)$; $\delta_u = -3^o$; $\delta_{au} = 0^o$; $\delta_l = 0^o$; $\delta_{rb} = 0^o$; $\delta_r = 0^o$.
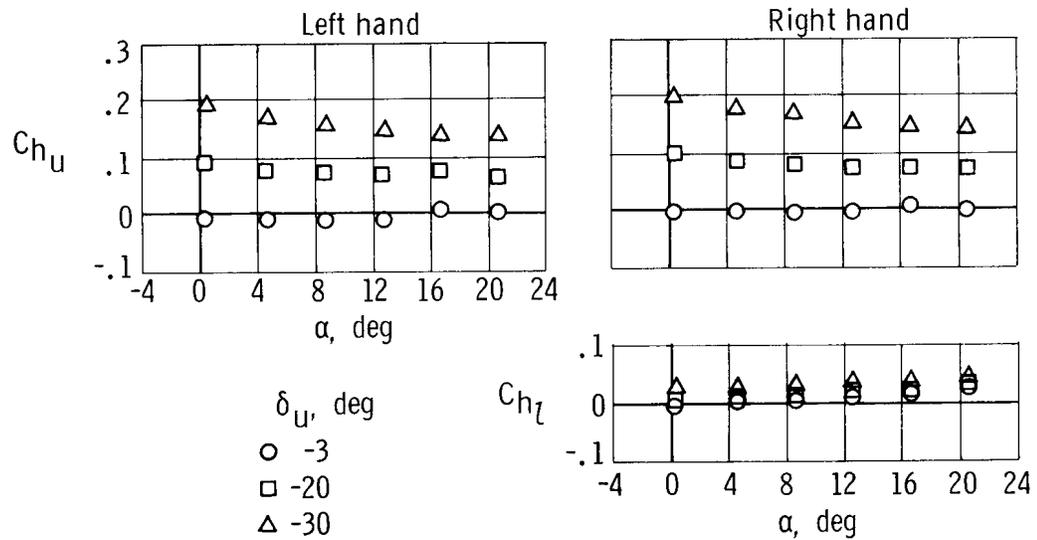

(g) Simulated ablated-coating and dynamic-pressure effect; $\beta = 0^o$; $\delta_u = -20^o$; $\delta_{au} = 0^o$; $\delta_l = 10^o$; $\delta_{rb} = -9^o$; $\delta_r = 0^o$.
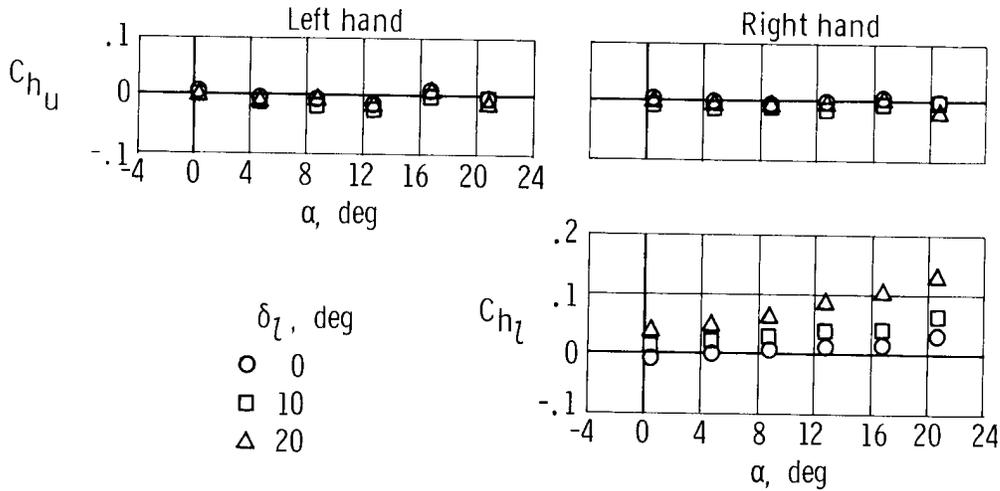
Figure 6.— Concluded.

(a) Rudder-bias effect; $q = 100 \ lb/ft^2 \ (4790 \ N/m^2)$; $\beta = 0^o$; $\delta_u = -20^o$; $\delta_{au} = 0^o$; $\delta_l = 10^o$; $\delta_r = 0^o$.
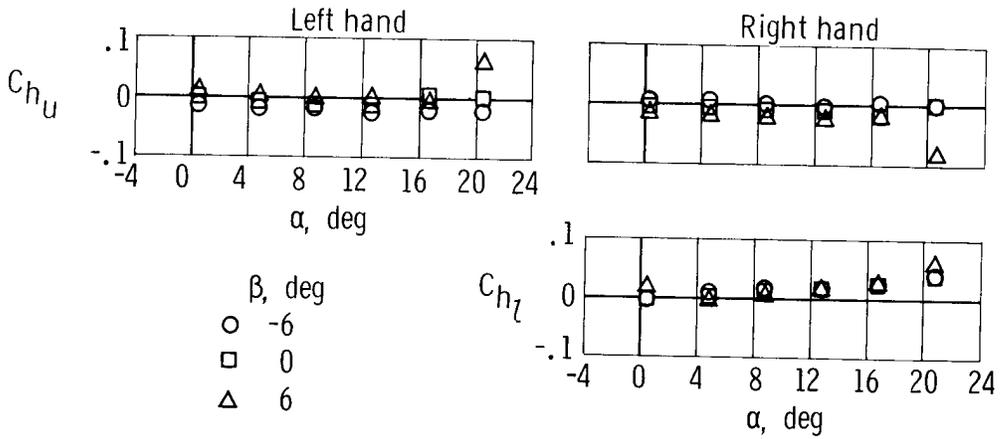
(b) Upper-flap effect; $q = 100 \ lb/ft^2 \ (4790 \ N/m^2)$; $\beta = 0^o$; $\delta_{au} = 0^o$; $\delta_l = 0^o$; $\delta_{rb} = 0^o$; $\delta_r = 0^o$.

Figure 7.— Variation of upper- and lower-flap hinge-moment coefficients with angle of attack.

Left hand   Right hand

C_{h_u}

C_{h_l}

α, deg

δ_l, deg
- O 0
- □ 10
- △ 20

(c) Lower-flap effect; $q = 100 \ lb/ft^2 \ (4790 \ N/m^2)$; $\beta = 0^o$; $\delta_u = -3^o$; $\delta_{au} = 0^o$; $\delta_{rb} = 0^o$; $\delta_r = 0^o$.

Left hand   Right hand

C_{h_u}

C_{h_l}

α, deg

β, deg
- O -6
- □ 0
- △ 6

(d) Sideslip-angle effect; $q = 100 \ lb/ft^2 \ (4790 \ N/m^2)$; $\delta_u = -3^o$; $\delta_{au} = 0^o$; $\delta_l = 0^o$; $\delta_{rb} = 0^o$; $\delta_r = 0^o$.

Left hand   Right hand

C_{h_u}

C_{h_l}

α, deg

q, lb/ft^2 (N/m^2)
- O 100 (4790)
- □ 80 (3830)
- △ 60 (2870)
- ◇ 60 (2870) ablated
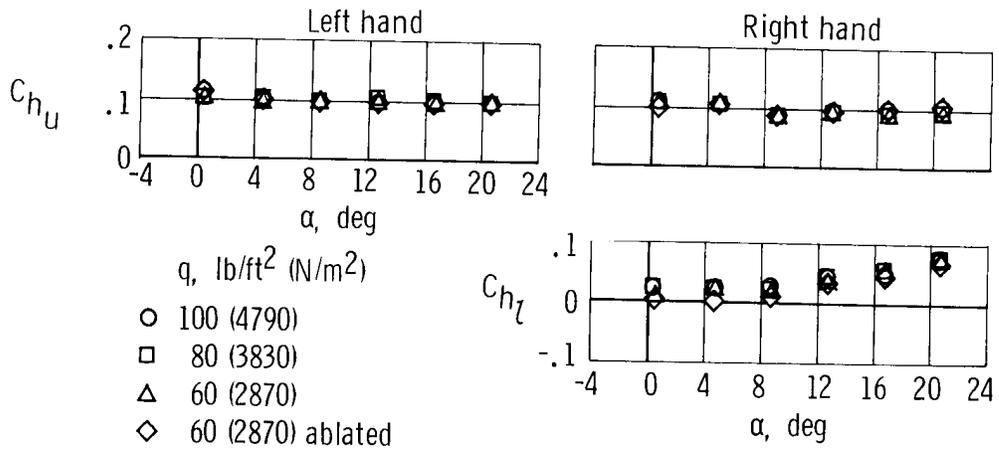
(e) Simulated ablated-coating and dynamic-pressure effect; $\beta = 0^o$; $\delta_u = -20^o$; $\delta_{au} = 0^o$; $\delta_l = 10^o$; $\delta_{rb} = -9^o$; $\delta_r = 0^o$.
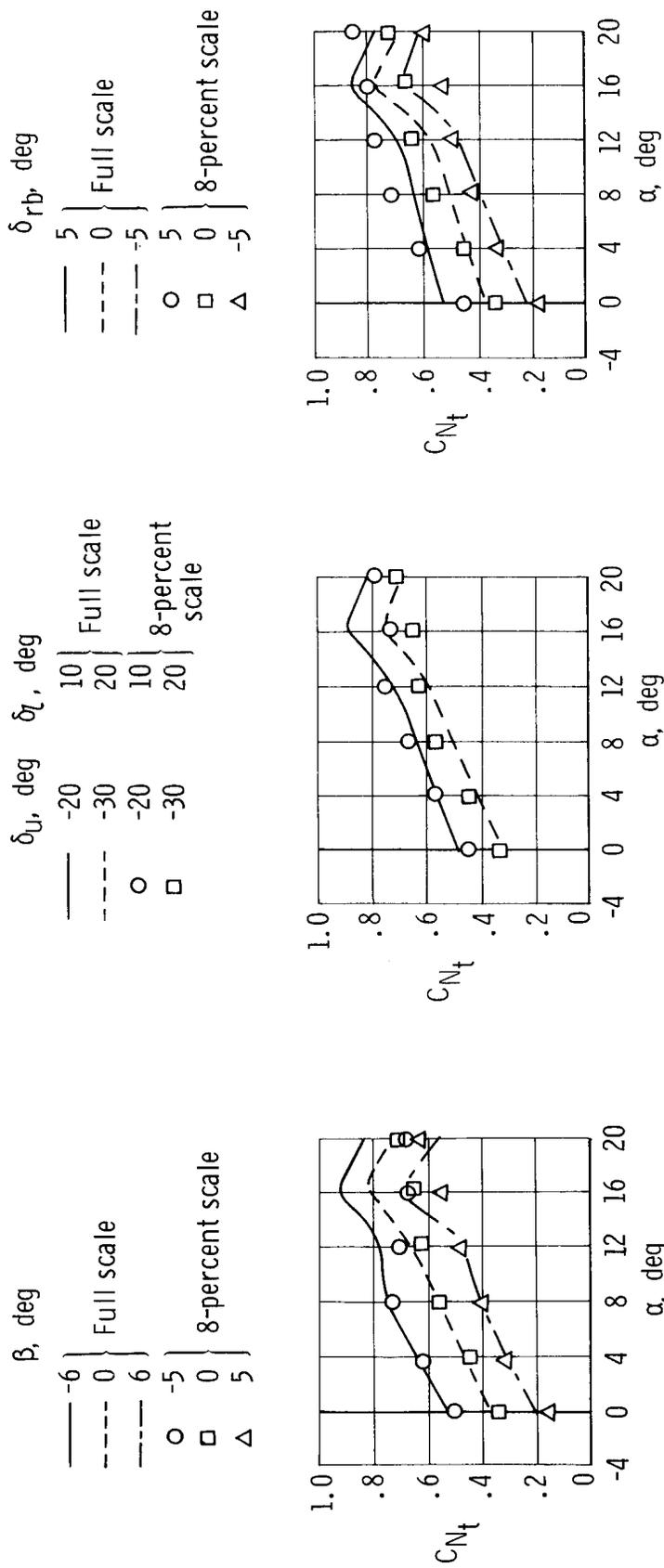
Figure 7.— Concluded.

Figure 8.— Comparison of left-hand outboard-fin normal-force coefficients from full-scale-model and 8-percent-scale-model wind-tunnel tests.

(a) Sideslip-angle effect; M = 0.25, full scale; M = 0.6, 8-percent scale; $\delta_u = -30^o$; $\delta_l = 20^o$; $\delta_{rb} = 0^o$; $\delta_r = 0^o$.

(b) Upper- and lower-flap effect; M = 0.25, full scale; M = 0.6, 8-percent scale; $\beta = 0^o$; $\delta_{rb} = 0^o$; $\delta_r = 0^o$.

(c) Rudder-bias effect; M = 0.25, full scale; M = 0.6, 8-percent scale; $\beta = 0^o$; $\delta_u = -30^o$; $\delta_l = 20^o$; $\delta_r = 0^o$.
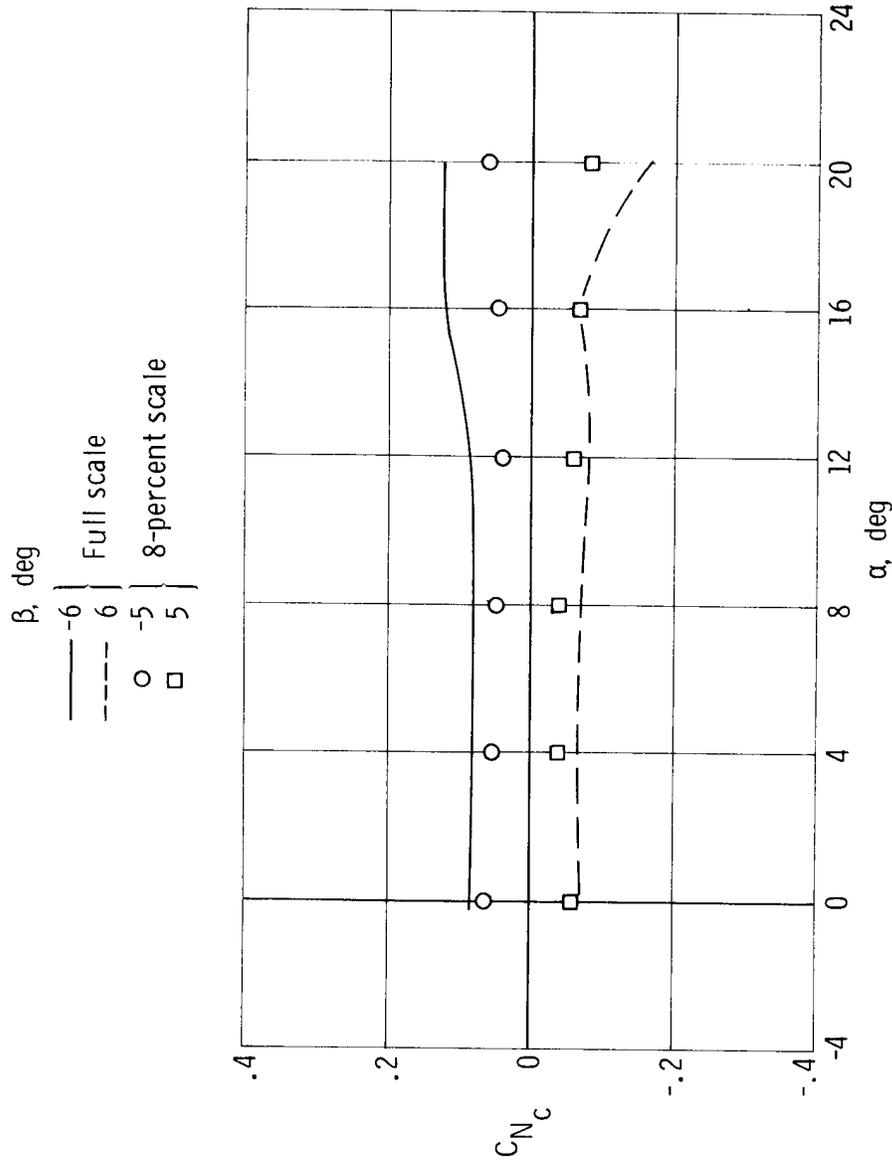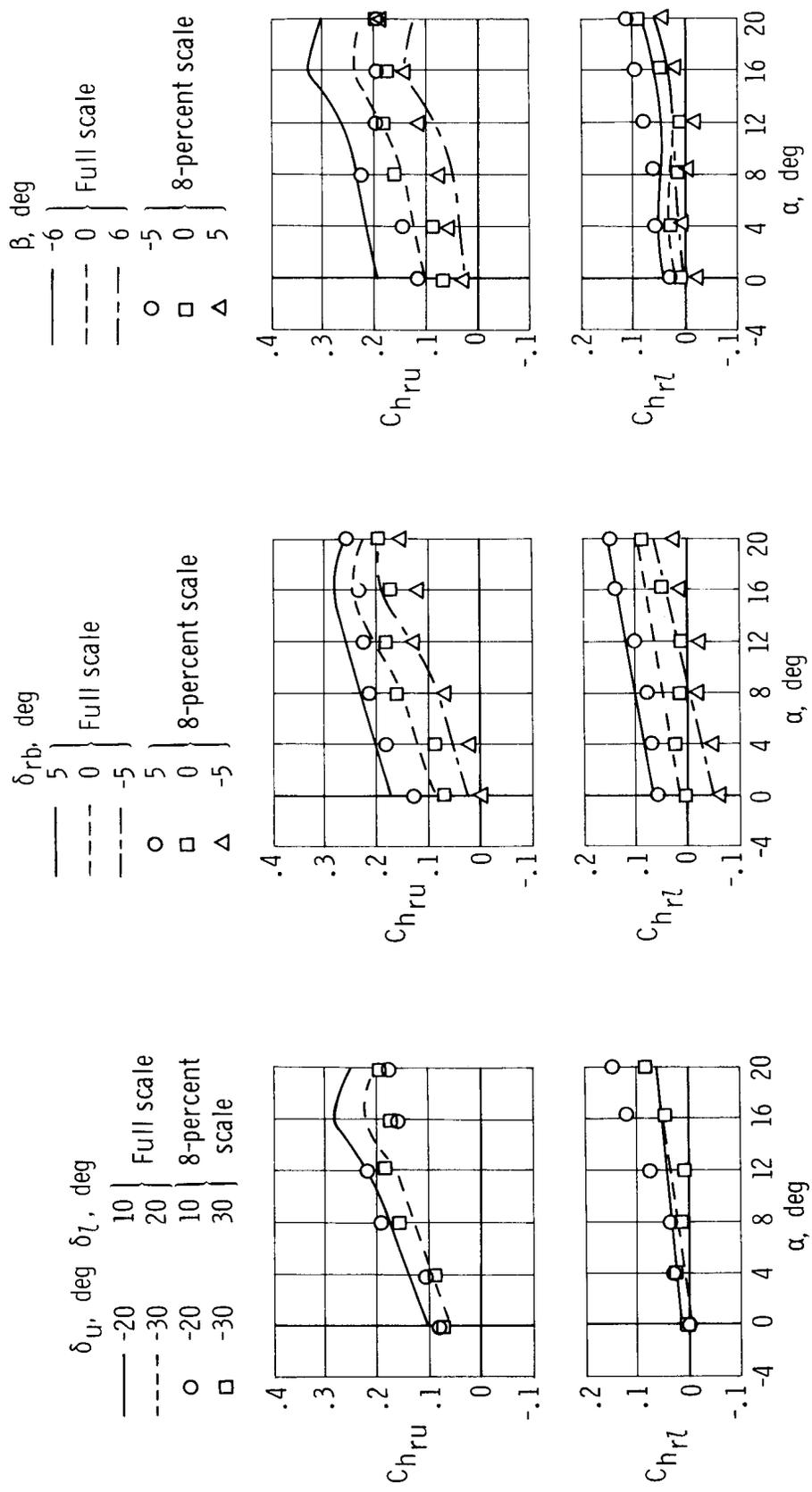
31

Figure 9.— Comparison of center-fin normal-force coefficients from full-scale-model and 8-percent-scale-model wind-tunnel tests showing effect of sideslip-angle variation. $\delta_{rb} = 0^o$; $\delta_r = 0^o$; full scale: $M = 0.25$, $\delta_u = -3^o$, $\delta_l = 0^o$; 8-percent scale: $M = 0.6$, $\delta_u = -30^o$, $\delta_l = 20^o$.

Figure 10.– Comparison of left-hand upper- and lower-rudder hinge-moment coefficients from full-scale-model and 8-percent-scale-model wind-tunnel tests.

(a) Upper- and lower-flap effect; $M = 0.25$, full scale; $M = 0.6$, 8-percent scale; $\beta = 0^o$; $\delta_{rb} = 0^o$; $\delta_r = 0^o$.

(b) Rudder-bias effect; $M = 0.25$, full scale; $M = 0.6$, 8-percent scale; $\beta = 0^o$; $\delta_u = -30^o$; $\delta_l = 20^o$; $\delta_r = 0^o$.

(c) Sideslip-angle effect; $M = 0.25$, full scale; $M = 0.6$, 8-percent scale; $\delta_u = -30^o$; $\delta_l = 20^o$; $\delta_{rb} = 0^o$; $\delta_r = 0^o$.

(a) Upper- and lower-flap effect; $M = 0.25$, full scale; $M = 0.6$, 8-percent scale; $\beta = 0^o$; $\delta_{rb} = 0^o$; $\delta_r = 0^o$.

(b) Rudder-bias effect; $M = 0.25$, full scale; $M = 0.6$, 8-percent scale; $\beta = 0^o$; $\delta_u = -30^o$; $\delta_l = 20^o$; $\delta_r = 0^o$.

(c) Sideslip-angle effect; $M = 0.25$, full scale; $M = 0.6$, 8-percent scale; $\delta_u = -30^o$; $\delta_l = 20^o$; $\delta_{rb} = 0^o$; $\delta_r = 0^o$.
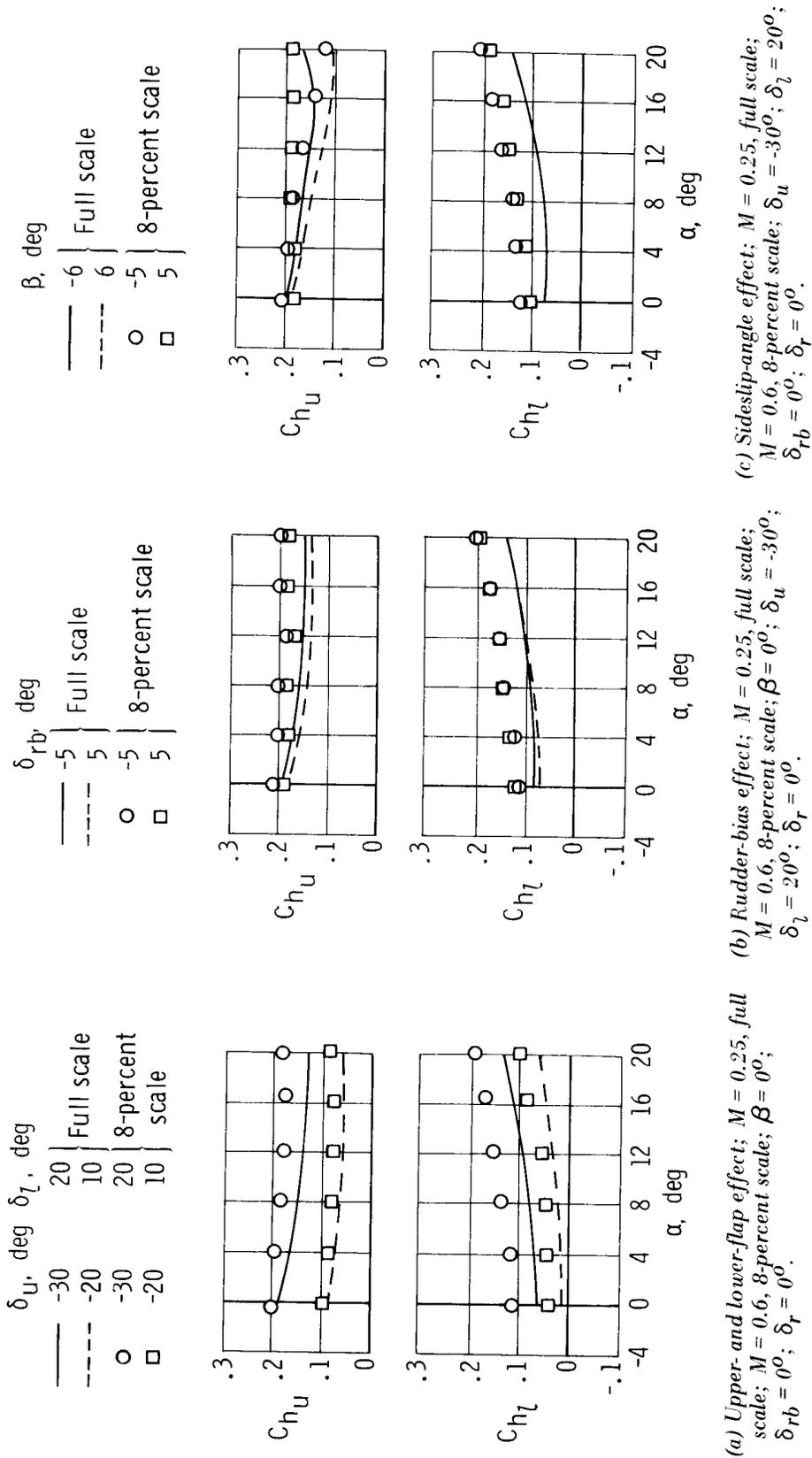
Figure 11.— Comparison of upper- and lower-flap hinge-moment coefficients from 8-percent-scale-model and full-scale-model wind-tunnel tests.